Rock and Soil Mechanics

Volume 42 | Issue 1 Article 2

5-26-2021

Experimental study of generalized stress relaxation of rock based on 3D-DIC technology

Jiang XU
State and Local Joint Engineering Laboratory of Methane Drainage in Complex Coal Gas Seam, Chongqing University, Chongqing 400044, China

Xiao-zheng SONG
State and Local Joint Engineering Laboratory of Methane Drainage in Complex Coal Gas Seam, Chongqing University, Chongqing 400044, China

Shou-jian PENG
State and Local Joint Engineering Laboratory of Methane Drainage in Complex Coal Gas Seam, Chongqing University, Chongqing 400044, China

Can-can CHEN
State and Local Joint Engineering Laboratory of Methane Drainage in Complex Coal Gas Seam, Chongqing University, Chongqing 400044, China

See next page for additional authors

Custom Citation

XU Jiang, SONG Xiao-zheng, PENG Shou-jian, CHEN Can-can, RAN Xiao-meng, YAN Fa-zhi, . Experimental study of generalized stress relaxation of rock based on 3D-DIC technology[J]. Rock and Soil Mechanics, 2021, 42(1): 27-38.

Experimental study of generalized stress relaxation of rock based on 3D-DIC technology

Authors

Jiang XU, Xiao-zheng SONG, Shou-jian PENG, Can-can CHEN, Xiao-meng RAN, and Fa-zhi YAN

Rock and Soil Mechanics 2021 42(1): 27−38 ISSN 1000−7598
https: //doi.org/10.16285/j.rsm.2020.5816 rocksoilmech.researchcommons.org/journal

Experimental study of generalized stress relaxation of rock based on 3D-DIC technology

XU Jiang[1, 2], SONG Xiao-zheng[1, 2], PENG Shou-jian[1, 2], CHEN Can-can[1, 2], RAN Xiao-meng[1, 2], YAN Fa-zhi[1, 2]

1. State Key Laboratory of Coal Mine Disaster Dynamics and Control, Chongqing University, Chongqing 400044, China
2. State and Local Joint Engineering Laboratory of Methane Drainage in Complex Coal Gas Seam, Chongqing University, Chongqing 400044, China

Abstract: Based on the visual triaxial compression servo-control test system and the three-dimension digital image correlation technology (3D-DIC), the generalized stress relaxation tests under different rheological regions were carried out, and the evolution of strain in the rock surface was discussed. The experimental results show that if sandstone tends to fail during the rheological process, the axial and radial strain concentration area would gradually appear in strain fields. The axial strain concentration area concentrates from the layered discrete distribution to the position of the upcoming crack, while the radial strain concentration area is about to form with the centered crack. The differential evolution rates of axial and radial strains at different areas are positively correlated with the overall strain evolution rate. The development of axial and radial strain in cement near the crack is going through three stages: deceleration, constant velocity and acceleration. The strain in areas away from the crack may increase firstly and then decrease. And the isochronous curve of the strains at different positions indicates the area where the crack is about to form. As the rheological direction coefficient α changes from 0.3, 0, −3.0, ∞, and 3.0 in sequence, the mean and variance of the overall evolutions of the axial and radial strain fields increase during the rheological process, indicating that the evolution rate is accelerated, the strain concentration phenomenon is more significant, and the difference between the evolution of the strain field before and after the sandstone failure also increases.

Keywords: generalized stress relaxation; three-dimension digital image correlation; surface strain field; strain evolution

1 Introduction

In the process of rheology, the mineral fabric of rock mass is constantly reorganized under external load, so that the strain evolution is not initiated and complete instantaneously, and the deformation is not uniformly distributed. When the deformation of rock mass in the weak area reaches the threshold, instable failure would occur, which affects the overall rheological strength characteristics[1−2]. In practical engineering, such as the phenomenon of zonal fracture of surrounding rock after deep excavation, the large deformation of the roadway still exceeds the anchorage limit under the corresponding support. The process of zonal fracture of surrounding rock is commonly accompanied by the redistribution of stress and displacement in several adjacent areas, and therefore in the similar engineering background, the mechanical properties of rock mass in the rheological process need to be carefully considered[3−4]. At present, the research on rock rheological properties mainly focuses on the creep and stress relaxation characteristics [4−11]. However, due to the anisotropy of rock mass and the complexity of engineering environment, the application of the creep and stress relaxation theory to explaining the rheological mechanical behavior of rock mass is limited by non-linearity[12−13]. Fukui et al.[14] defined the rheological state of rock with simultaneous changes in stress and strain as generalized stress relaxation, which was used to explain the general rheological characteristics of engineering rock mass. Hashiba et al. [15] carried out load rate dependence and generalized stress relaxation tests on granite and studied the time effect of granite. He numerically calculated the load rate dependence curve and generalized stress relaxation curve with the improved elasto-viscous constitutive equation. Xu et al.[16] carried out the generalized stress relaxation tests of tuff under different confining pressures. The results show that when the axial strain increases, the higher the confining pressure is, the more difficult the axial deformation is. When the strain decreases, the higher the confining pressure is, the more obvious the deformation of rock specimen is.

In addition, due to the anisotropy and other unique characteristics of the rock, the deformation is not uniform under external load. The strain localization phenomenon

Received: 14 June 2020 Revised: 27 September 2020
This work was supported by the National Natural Science Foundation of China (51874055，51974041), and the Chongqing Special Postdoctoral Science Foundation (XmT2018005).
First author: XU Jiang, male, born in 1960, PhD, Professor, PhD supervisor, mainly engaged in rock mechanics and engineering teaching and research. E-mail: jiangxu@cqu.edu.cn

occurs after the deformation reaches a critical threshold, which cannot be measured accurately by contact measurement method. However, Digital Image Correlation (DIC) technology is a non-contact optical measurement method that facilitates us to analyze such phenomenon. Xing et al. [17] used 3D-DIC technology to analyze the evolution rule of the surface deformation field of sandstone under dynamic load. The propagation rule of the pre-peak strain field, and the correlation between the failure of post-peak rock and the strain rate, as well as the strain localization phenomenon were also be analyzed. Munoz et al. [18] used 3D-DIC technology to investigate the post-peak mechanical strength characteristics of sandstone with different aspect ratios under uniaxial compression, and analyzed the deformation localization characteristics of axial and shear strain fields. Using 3D-DIC technology, Tang et al.[19] analyzed the progressive failure process of rock under different confining pressures. Based on the difference of strains inside and outside the strain localization zone, they found that with the increase of confining pressure, the initiation stage of rock strain localization was delayed. Based on DIC technique, Wang et al.[20] analyzed the strain localization phenomenon of coal in the process of uniaxial compression. They combined the strain difference coefficient in the strain field with the axial strain, and suggested that with the increase of axial strain, the strain localization zone gradually developed from fuzzy to clear and narrowed. Song et al. [21] analyzed the surface deformation field of red sandstone in the creep process under graded loading, and discussed the fracture development in the creep process of rock under various stress levels, as well as the change of strain in the area inside and outside the fracture after the deformation reaches the critical value.

At present, due to the non-visual design of most rock triaxial compression testing machines, the applications of DIC technology in the field of rock mechanics are mainly focusing on uniaxial compression and splitting load tests. However, there are few reports on the rheological deformation characteristics of rock under triaxial compression based on 3D-DIC. In this study, based on the visualization triaxial compression servo control test system that can carry out the generalized stress relaxation tests, combined with the 3D reconstruction advantage of 3D-DIC technology in the analysis of non-plane specimens, different generalized stress relaxation tests are carried out. The evolution rule of strain field on rock surface during rheological process is analyzed.

2 Generalized stress relaxation test method based on 3D-DIC

2.1 Composition of test system

Based on 3D-DIC technology, the author's team improved the visual triaxial compression servo control testing system [22] that could carry out the generalized stress relaxation test, and realized the measurement of the surface deformation evolution of rock samples in the process of generalized stress relaxation under the conventional triaxial compression load. Figure 1 is the photo of the improved testing system. It is mainly composed of loading system, servo control system, visual triaxial pressure chamber, 3D-DIC system and test acquisition system. The maximum axial load of the loading system is 500 kN, the maximum confining pressure and the maximum fluid pressure are 10 MPa and 50 MPa, respectively. Servo control system is driven by waveform generator instruction. The servo valve is controlled by signal combination through the signal amplifier and the variable resistor. The output power of the servo valve is adjusted based on the force sensor at the bottom of the fixed support and the force and displacement signal input by the axial displacement sensor at the top of the hydraulic cylinder. In this way, the stress recycle control is realized. The transparent confining pressure chamber of the visualized triaxial stress chamber has an outer diameter of 100 mm, an inner diameter of 30 mm, and a height of 70 mm. The refractive index of the molding material against light is 1.49. 6 bolts are evenly distributed outside the transparent confining pressure chamber to connect the upper and lower metal plates. The confining pressure chamber contains a loading rod and a lower pad. The loading rod is 25 mm in diameter and allows fluid to pass through. The 3D-DIC system is composed of an image acquisition system, an image analysis control system and a calibration system. In the image acquisition system, 6 industrial cameras with images up to 2 448 pixels ×2 048 pixels are distributed in pairs around the triaxial stress chamber. In the calibration system, a tri-prism coded calibration plate and a small central calibration plate are customized

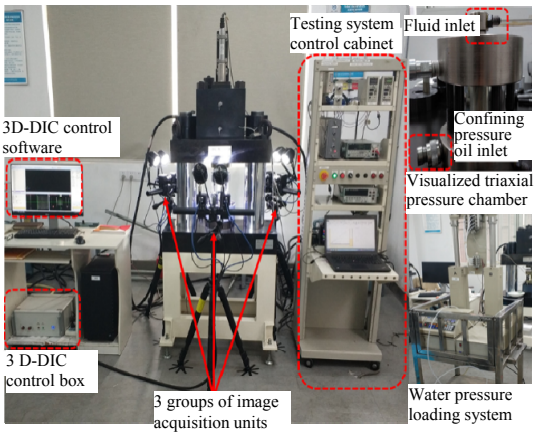

Fig. 1 Visual triaxial compressive servo-control testing system

for the establishment of spatial coordinates and correction of the calibration results affected by hydraulic oil and transparent pressure chamber. The experimental acquisition system realizes the synchronous acquisition of force sensor, displacement sensor and industrial camera.

2.2 Test method and reliability discussion

The measurement principle of 3D-DIC is mainly based on digital image matching technique and binocular stereo vision technique[23]. Binocular stereo vision technique uses dual lenses to determine the spatial position of pixel points on the surface of an object. Through image gray processing, digital image matching technique transfers speckle images with different time dependent physical features into digital images, and then develops analysis area and correlation algorithm based on the digital images. According to the initial reference image, the correlation calculation of the subsequent images in the analysis area is carried out, and finally the deformation information of the target object in the 3D space is determined. After that, the strain on the inner surface of each region at each time can be analyzed. The virtual strain gauges with different directions can be arranged at different positions to obtain strain values in multiple directions. As shown in Fig. 2, the surface deformation analysis area of the three observation surfaces (L1, L2 and L3) (corresponding to a 3D plane with a height of about 40 mm, an arc length of about 20 mm and a radian of about 110° on the surface of the specimen) can comprehensively reflect the strain differences of various regions on the rock surface. In order to make full use of 3D-DIC system to analyze the evolution rule of strain of sandstone during the rheological process, the author finally selected 5 axial and radial virtual strain gauges of equal length at equal distance in three analysis areas respectively. R1−R5 on each plane of L1, L2 and L3 are 15 virtual strain gauges in radial direction, respectively, and A1−A15 are 15 virtual strain gauges in axial direction, respectively.

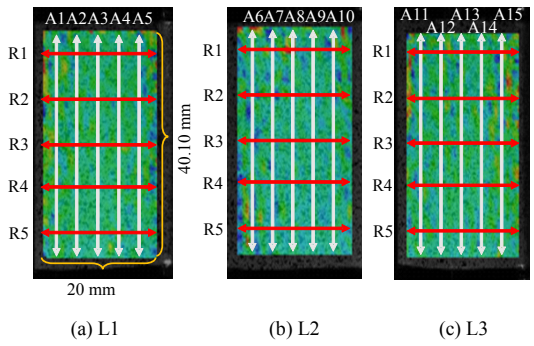

Fig. 2 Arrangement of virtual strain gauges

In view of the reliability of the measurement results of the 3D-DIC system, both strain gauges and 3D-DIC were used in the earlier stage to measure the deformation of the rock samples at the same time. The compression test was conducted at a constant rate to verify the reliability of the 3D-DIC measurement data in the test system[23]. In order to further discuss the measurement characteristics of 3D-DIC in the process of generalized stress relaxation of rock surface deformation, this paper analyzes the reliability of the measurement results of 3D-DIC system in the creep test of sandstone with 80% peak strength. Based on the analysis of DIC technology, some scholars obtained the average value of surface strain and performed relevant analysis[24]. In this paper, the entire evolutions of mean axial and radial strain in the whole test process are also obtained in the analysis areas of the three rock surface deformation fields, and are further compared with the strain evolution rule measured by the axial displacement sensor (LVDT) in the test system, as shown in Fig. 3. Figure 3(a) shows the axial stress ($\sigma_1-\sigma_3$)−axial strain (ε_1) curve in the whole creep test process, and Fig. 3(b) presents the strain variation ($\Delta\varepsilon_1$)−time (t) curve in the creep process. It can be seen that no matter in the stress loading stage or the subsequent rheological stage, the axial strain measured by LVDT is relatively larger than the mean value of surface axial strain measured by 3D-DIC. However, the strain increments of the two methods in the loading and rheological stages follow a certain proportional relationship. It can be inferred that the reason for the difference between the two measurement methods is mainly related to the axial deformation measured by LVDT, including the deformation of the loading rod and matching pad in the pressure chamber, which cannot be accurately estimated and excluded when calculating the axial strain of rock by LVDT. This leads to a higher axial strain than real rock. However, the 3D-DIC system obtains the average axial strain actually generated in different areas on the rock surface. Therefore, in the subsequent analysis, the rock surface deformation calculated by 3D-DIC system is used as the main data to analyze the generalized stress relaxation of rock.

2.3 Test scheme and procedure

The sandstone sample used in this paper was collected from the Xujiahe Formation of the Upper Triassic in Jingkou Town, Chongqing. The main components are quartz, feldspar, flint and muscotile, etc., and the pores in the sample are evenly distributed. After coring, cutting and grinding, the sandstone sample was processed into a cylindrical specimen with a size of Φ25 mm×50 mm, and the flatness of the end face was within 0.05 mm. The basic parameters of the sample (the mean value) are listed in Table 1.

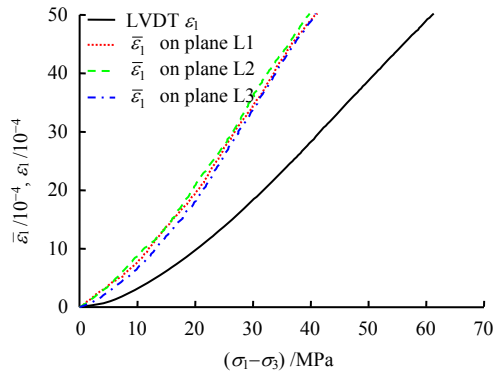

(a) Axial stress−axial strain throughout the test

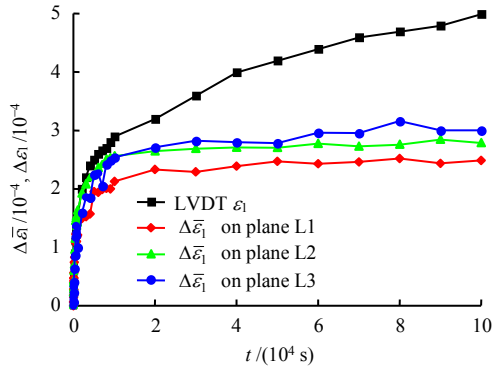

(b) Axial strain−time curves during creep process

Fig. 3 Measurement results of LVDT and DIC systems

Table 1 Physical and mechanical parameters of Jingkou-sandstone

Sample	Density /(g • cm^{-3})	Longitudinal wave velocity /(m • s^{-1})	Confining pressure /MPa	Elastic modulus /GPa	Compressive strength /MPa
Jingkou sandstone	2.27	3197.41	3	9.37	66.63

The previous research results of author's team discussed the engineering physical significance represented by different generalized stress relaxation coefficients α (the correlation constant of the ratio between $\Delta\varepsilon_1$ and $\Delta\sigma_1$) [16, 22]. On this basis, 80% of the axial peak strength of Jingkou Sandstone under 3 MPa confining pressure was selected as the starting point stress level of the generalized stress relaxation test. Five generalized stress relaxation tests were carried out at the rheological direction coefficients α of 3.0, ∞, −3.0, 0 and 0.3, respectively. The specific test scheme is shown in Table 2.

Table 2 Test schemes

Lithology	Rheological direction coefficient α	Seepage pressure /MPa	Rheological starting stress level	Confining pressure /MPa
Jingkou Sandstone	3.0 (Region I)	1	80% peak strength	3
Jingkou Sandstone	∞ (Creep)	1	80% peak strength	3
Jingkou Sandstone	−3.0 (Region II)	1	80% peak strength	3
Jingkou Sandstone	0 (Stress relaxation)	1	80% peak strength	3
Jingkou Sandstone	0.3 (Region III)	1	80% peak strength	3

(1) The prepared and selected rock samples were sprayed with matte paint to make artificial speckles with black spots on the surface of the sample. After drying, the spray paint was fully fitted to the surface of the rock sample and then placed in a vacuum vessel filled with water. The vacuum pump was used to pump the vessel to a negative pressure below 98 kPa. After maintaining for 48 h, the test was ready to carry out.

(2) Check the test system and set the control parameters, place the saturated rock sample between the upper and lower matching end blocks of the triaxial pressure chamber. Cover the transparent heat shrinkable tube and then use the heat gun to evenly blow tight. Use strong glue to seal the gap between the heat shrinkable tube and the end blocks. After the glue was fully solidified, put the sample into the pressure chamber and assembled the triaxial pressure chamber.

(3) After placing the triaxial pressure chamber in an appropriate position and applying 3 MPa axial stress and confining pressure, the hydraulic loading system was connected and the seepage pressure was applied to the preset value at a rate of 0.5 MPa/min. After water pressure kept constant for one hour, the test loading system and data acquisition system were started synchronously. The generalized stress relaxation test was started after the axial load was applied to the preset starting point axial stress, and the test was scheduled to stop after 10^5 s.

2.4 Control parameters evolution during the test

The key to carry out the generalized stress relaxation test is to ensure that the evolution rule of rock stress and strain conforms to the preset rheological direction coefficient, α, and the stability of axial load and axial displacement control. The data of the two parameters are from the force signal sensor (Loadcell) and displacement signal sensor (LVDT) of the test loading system.

2.4.1 Relation curve of axial stress−axial strain

Figure 4 shows the relation curve between axial stress $(\sigma_1-\sigma_3)$ and axial strain $\varepsilon_{1(\mathrm{LVDT})}$ under different test conditions. Curve 6 depicts the stress−strain curve in the loading process, and Curves 1−5 represent the generalized stress relaxation tests under different rheological direction coefficients after rheology. In the amplified figure, $\Delta\varepsilon_{1(\mathrm{LVDT})}$ on X axis and $\Delta(\sigma_1-\sigma_3)$ on Y axis represent the changes of axial strain and axial stress at the beginning of generalized stress relaxation, respectively. The stress−strain evolution rule of each rheological direction coefficient conforms to the rheological direction coefficient involved in the test scheme. Even in the tests where rheological direction coefficient are 3.0 and ∞, the development trends of axial stress and axial strain

before the failure of rock sample still maintain at the preset rheological direction coefficient.

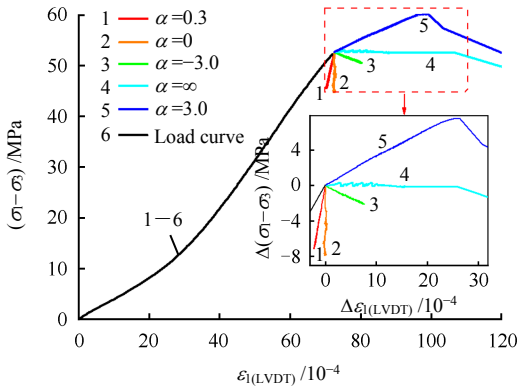

Fig. 4 Axial stress-strain curves in general relaxation tests

2.4.2 Time history evolution curve of axial stress variation

Figure 5 displays the time−history curve of axial stress variation $\Delta(\sigma_1-\sigma_3)$ in different generalized stress relaxation tests during the whole process of rheological control. It can be seen that $\Delta(\sigma_1-\sigma_3)$ at the rheological direction coefficient α=0.3, α=0 and α=−3.0 gradually decreases with time during the rheological process. After the rapid decline in the initial rheological period, $\Delta(\sigma_1-\sigma_3)$ gradually shows a trend of decelerated decline and then remains stable. In the test where the rheological direction coefficient $\alpha=\infty$ (i.e., creep), $\Delta(\sigma_1-\sigma_3)$ basically remains unchanged before the failure of the rock sample, but fails to remain constant and rapidly decreases after the failure. In the test where the rheological direction coefficient α=3.0, $\Delta(\sigma_1-\sigma_3)$ gradually grows with time in the process of rheology, which undergoes deceleration stage, constant velocity stage and acceleration stage, and finally decreases sharply after the failure of rock sample.

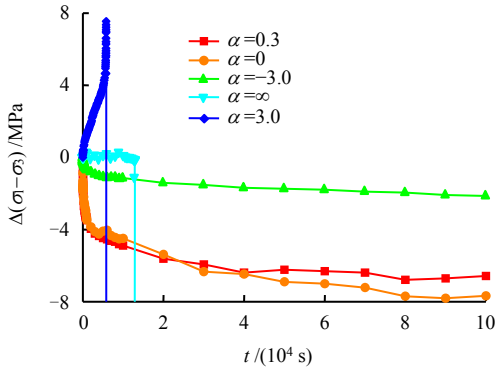

Fig. 5 Δ(σ1-σ3)-*t* curves in general relaxation tests

2.4.3 Time history evolution curve of axial strain variation

Figure 6 shows the time−history curve of axial strain variation $\Delta\varepsilon_{1(\mathrm{LVDT})}$ measured by LVDT in different generalized stress relaxation tests during the whole process of rheology. When the rheological direction coefficient α=0.3, $\Delta\varepsilon_{1(\mathrm{LVDT})}$ gradually decreases with time and then tends to be stable. In the test where α=0 (i.e., stress relaxation), $\Delta\varepsilon_{1(\mathrm{LVDT})}$ remains constant during the rheological process. When α=−3.0, $\Delta\varepsilon_{1(\mathrm{LVDT})}$ gradually increases with time and the rate of increase slows down gradually. However, the increases of $\Delta\varepsilon_{1(\mathrm{LVDT})}$ in the test of $\alpha=\infty$ and 3.0 are the same as that of $\Delta(\sigma_1-\sigma_3)$, which also experiences deceleration stage, constant velocity stage and acceleration stage, and finally rises rapidly after the failure of rock sample.

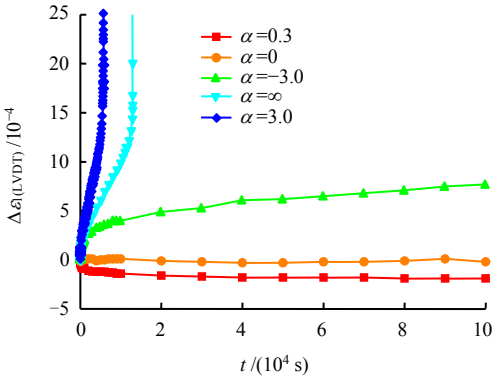

Fig. 6 Δε1(LVDT)-*t* curves in general relaxation tests

3 Strain field evolution of sandstone surface in generalized stress relaxation test

3.1 Evolution contour of axial strain field

Based on three acquisition units and analysis system of 3D-DIC system, the evolution rule of axial strain on three observation planes and the 3D distribution of strain contour in the process of generalized stress relaxation are obtained. The representative evolution contours are plotted in Fig. 7. The value of color bar is positive for tension and negative for compression. As can be seen from the contour at the initial stage of rheology, when loading to the starting stress level of rheology, in the axial contours under different test conditions, there are small regions with large axial strain, showing a red core and a yellow wrapped area, while the strain in other regions is relatively uniform and shows green. In addition, the red areas, wrapped in yellow, are roughly perpendicular to the axis and are layered distributed in strips. As a sedimentary rock, there is a certain degree of heterogeneity between layers in sandstone sample, and also the direction of drilling core is perpendicular to the bedding plane. This may cause the weaker layer to deform more non-uniformly than other denser areas under the axial load during the axial load loading process, that is, the axial strain field formed is more nonuniformly.

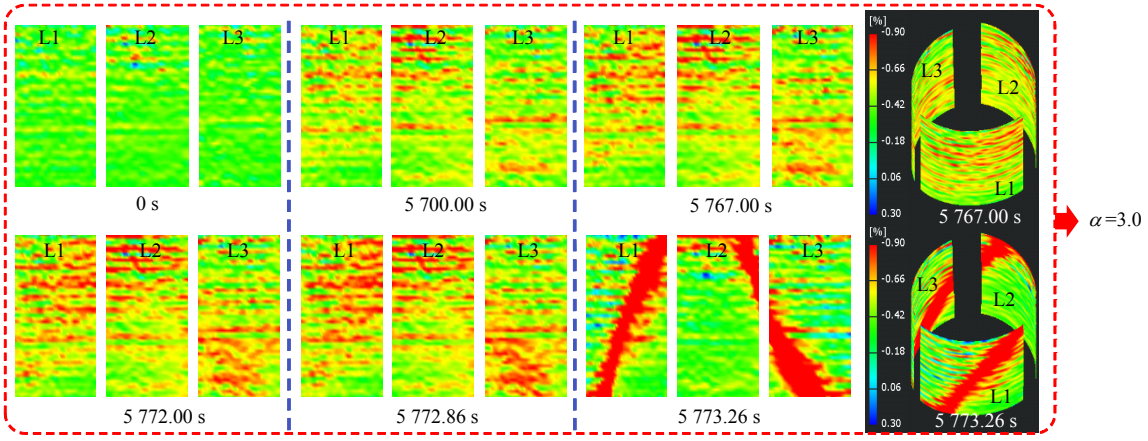

(a) α=3.0

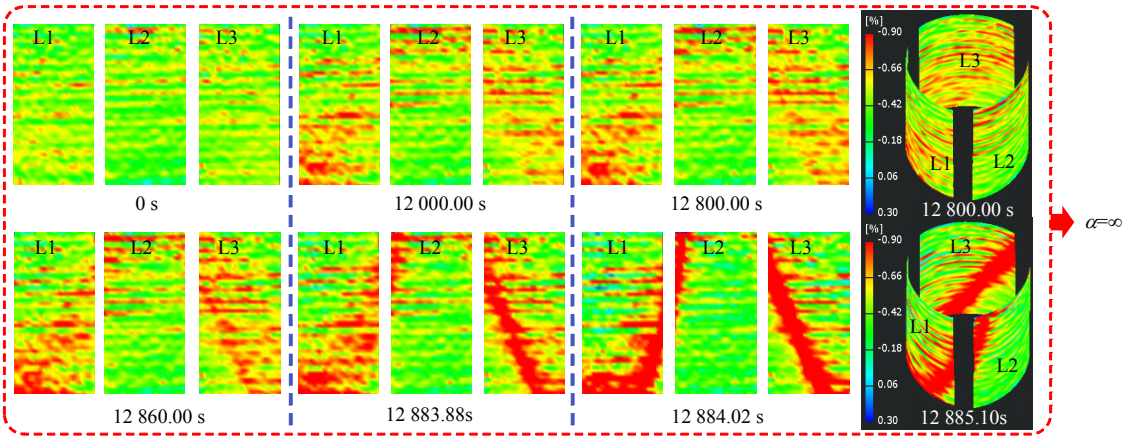

(b) α=∞

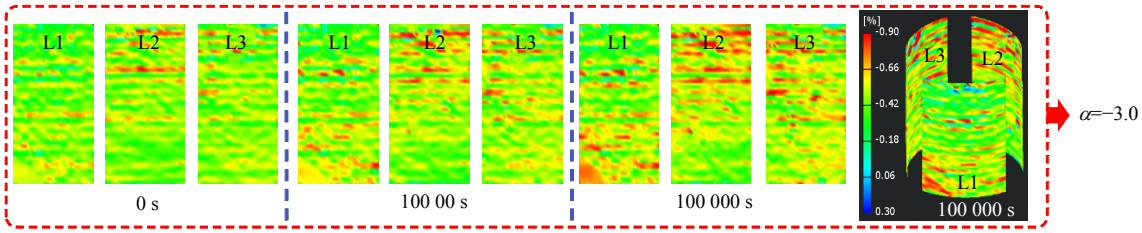

(c) α=−3.0

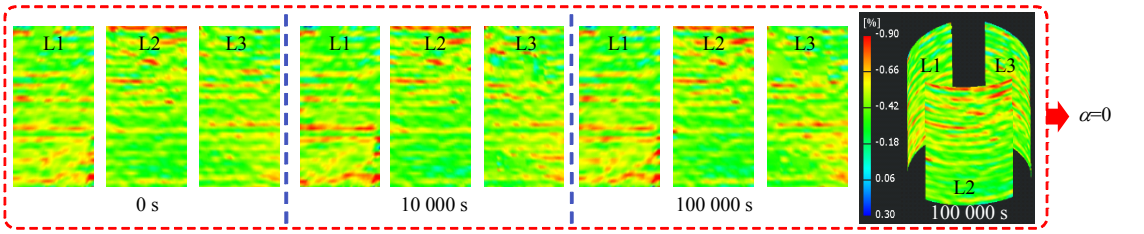

(d) α=0

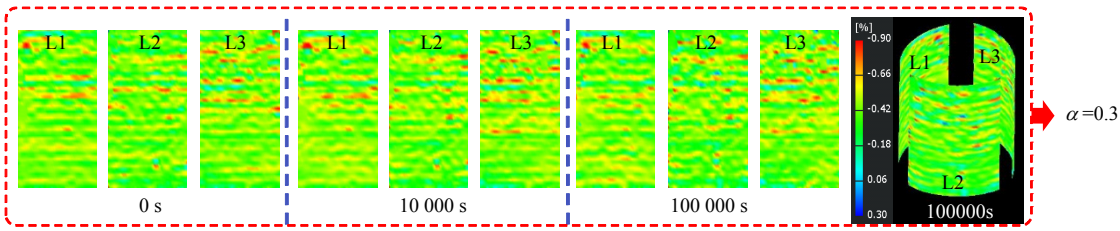

(e) α=0.3

Fig. 7 Axial strain contours of different directional coefficients in general relaxation tests

In the test with the rheological direction coefficient α of 3.0 and ∞, rock sample was damaged during the rheological process, as shown in Figs. 7(a) and 7(b). With the evolution of time, in the generalized stress relaxation test of α=3.0, after 5 700.00 s, a large quantity of red regions have appeared in the axial direction, and in the next 73.00 seconds, the increase rate of the red regions accelerates gradually, and the increase rate of the axial strain in some areas is much faster than that in others. In the 3D axial strain contour at 5 767.00 s, the spatial distribution is not obvious. In the last acquisition moment near to the formation of macro cracks (5 772.86 s), the proportion of red regions has changed significantly from the initial moment, but they are still distributed in layers in the form of strips. However, at the first acquisition moment after the formation of macro cracks, the distribution of red regions changes remarkably, and distinct oblique run-through red areas appear, while some red regions have changed into regions with small axial strain. The 3D axial strain contour at this time clearly shows the spatial correspondence of the red regions on the three observation planes, which is consistent with the location of the cracks actually forming in the sample. In Fig. 7(b), i.e., the generalized stress relaxation test of $\alpha=\infty$, red regions that are similar to that of $\alpha=$ 3.0 also appear at 12 000.00 s. In the subsequent evolution of 884.00 s, compared with the axial strain contour of α=3.0, the locations of the red regions are more concentrated and the rate of evolution is relatively slower. Similarly, in the two acquisition states before and after failure, the red regions in the axial strain contour are gradually concentrated. At the last acquisition moment (12 883.88 s) before the formation of macro cracks, the striped red regions have been connected to each other and formed a more concentrated red region. At the first acquisition moment (12 884.02 s) after the formation of macro cracks, a more obvious red axial strain concentration region is formed, while the axial strain value in some red areas restores to a smaller value. This red region in the 3D axial strain contour also corresponds to the location of the actual cracks forming in the rock sample. In comparison, it is revealed that under the same starting point axial stress level and water pressure, the axial strain concentration on the sample surface does not necessarily have the same development trend and the threshold value of crack formation before and after the formation of macro cracks.

As for the test with the rheological direction coefficient α=–3.0, in the evolution contour of axial strain as shown in Fig. 7(c), the region with a larger compressive strain value develops faster, and the yellow and red regions gradually increase. However, no connection between stripe strain concentration regions was found in the axial strain contour at the end of rheology test. In Figs. 7(d) and 7(e), there is no significant difference in the evolution of axial strain field at each rheological stage. This is mainly because the axial displacement in the generalized stress relaxation test in the direction of α=0 (i.e., stress relaxation) remains unchanged, and the axial load in the direction of α=0.3 decreases. Meanwhile, the corresponding axial displacement also decreases to a certain level, but this magnitude is small, therefore it is difficult to observe any significant evolutionary difference in the axial strain contour.

3.2 Evolution contour of radial strain field

Figure 8 illustrates the evolution law of 3D radial strain contour of sandstone in different generalized stress relaxation tests. The value of color bar is positive for tension and negative for compression. The selected time points for the images are corresponding to those of the axial strain contour. It can be seen that when the load reaches the rheological starting axial stress level, the entire sample surface presents tensile deformation, in which part of the region is green. Moreover, the tensile strain value is large and most of the region is cyan. Irregularly distributed compressive strain appears in individual regions, represented by colored areas below light blue.

It is known that in the tests with rheological direction coefficients α of 3.0 and ∞, rock sample is fractured during rheology. When the generalized stress relaxation test of α=3.0 reaches 5 700.00 s, most of the radial strain field has turned green, and a small part of the region even appears in yellow and red. After that, the proportion of yellow and red regions gradually increases. The red region is surrounded by the yellow region. As it can be seen from the 3D radial strain contour at 5 767.00 s, these regions are still distributed discretely in sample surface. In the last acquisition time before macro cracks formation (5 772.86 s), red regions still present scatteredly, but in the first acquisition time after sample failure (5 773.26 s), the distribution of the red regions shows significant changes. There is an obvious tilt and penetrating red region, surrounded by a small yellow region peripherally, and then a small green area outside. Similar to the evolution of the axial strain field, the radial tensile strain concentration occurs in less than 0.50 s, surrounding the region where the macro cracks are located. However, in the generalized stress relaxation test with $\alpha=\infty$, a small part of red and yellow regions also appear at 12 000.00 s, while other regions are mostly green. However, the development trends of the red and yellow regions are slower and gentler than that of the radial strain contour of α=3.0 in the following 884.00 s. At the last acquisition moment (12 883.88 s) near the macroscopic failure, a large red region with tensile strain concentration has been formed, which is much

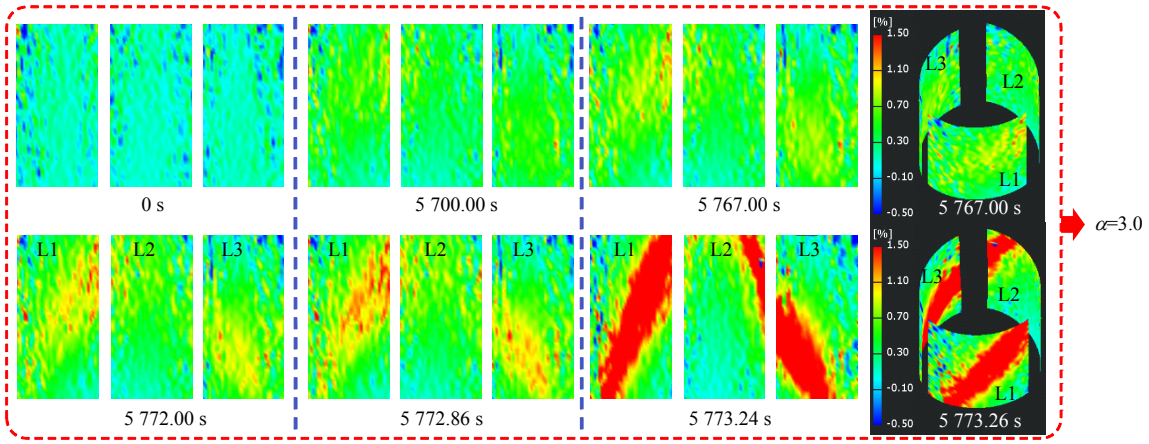

(a) α=3.0

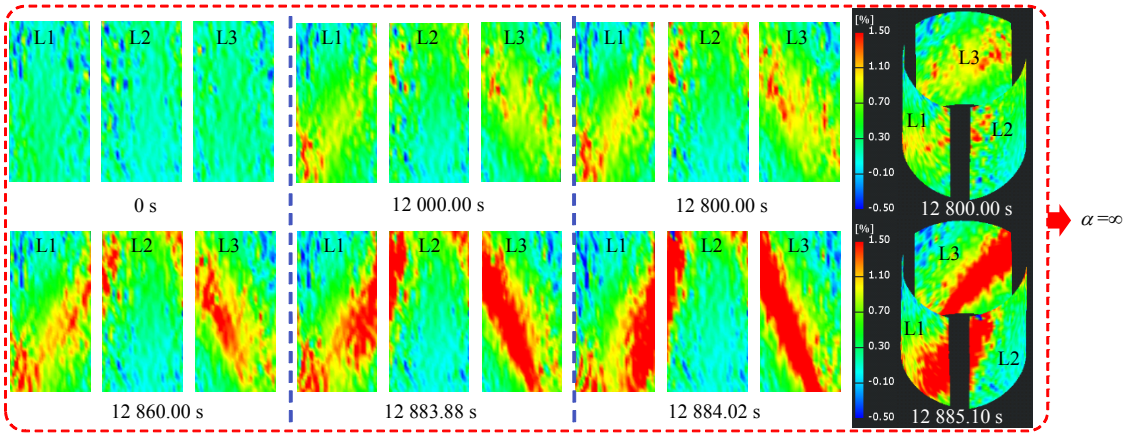

(b) α=∞

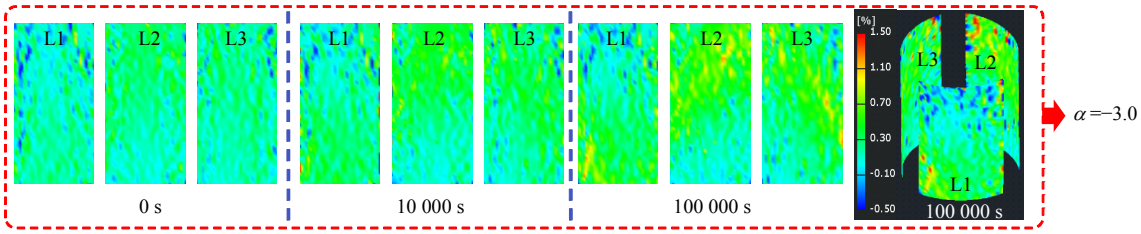

(c) α=−3.0

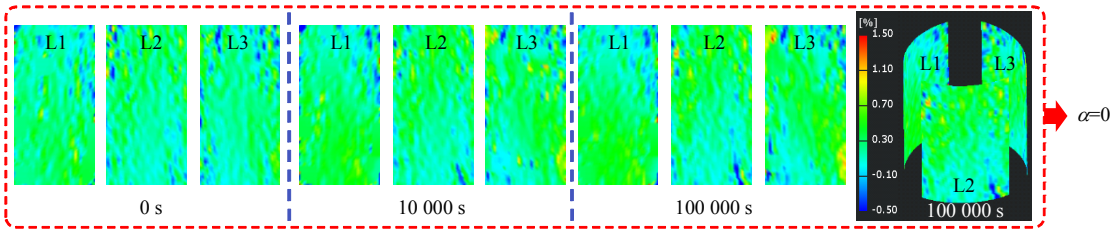

(d) α=0

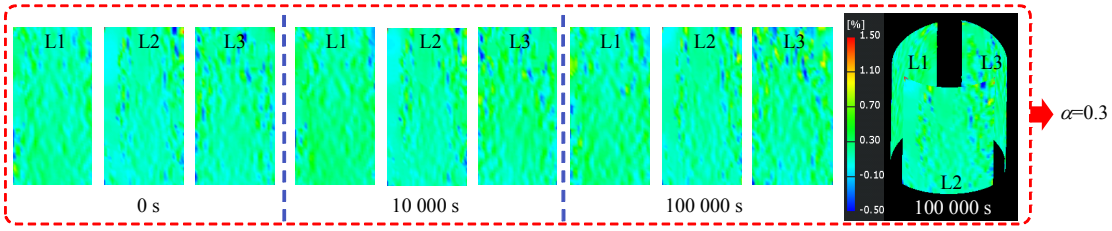

(e) α=0.3

Fig. 8 Radial strain contours of different directional coefficients in general relaxation tests

larger than the radial strain contour of α=3.0 before macro cracks formation. However, after the formation of macro cracks, the evolution difference between red and yellow regions is not as obvious as that of α=3.0. However, after the formation of macro cracks, the 3D radial strain contours of the two tests form strain concentration regions around the cracks, which is more obvious than the triaxial strain contour. When the rheological direction coefficient is −3.0 and 0 respectively, the radial strain field shows an overall trend of increasing tensile strain. Some regions gradually change from cyan to green, and thus the green area increases. Additionally, the green area at the initial time has a faster evolution rate. At the end of the rheology at 100 000 s, a small part of the yellow region has appeared. In the test with the rheological direction coefficient of 0.3, the green area increases to a certain extent from 0 to 10 000 s, but the radial strain field does not change significantly in the subsequent 90 000 s.

3.3 Quantitative analysis of surface strain field evolution

In order to quantitatively analyze the evolution rule of axial and radial strains on the rock sample surface during the rheological process, a series of virtual strain gauges was arranged as shown in Fig. 2. Due to the limitation of the article length, the creep test of sandstone is selected for display. Figure 9 shows the evolution curves of axial strain variation $\Delta\varepsilon_1$−time t as measured on each observation plane. It is clear that the 15 axial virtual strain gauges all show decline trends in the first 1 000 s, and then the difference in the axial strain variations at different positions gradually become obvious. During the period of 8 000−12 000 s, the $\Delta\varepsilon_1$ at A8, A9 and A10 of L2 plane does not change basically, and shows an accelerated decreasing trend in 884 s before the failure. In contrast, the $\Delta\varepsilon_1$ at other positions increases at a constant rate and then enters an accelerated growth stage. Figure 10 shows the evolution curves of radial strain variation $\Delta\varepsilon_3$ and time t measured from 15 virtual strain gauges in radial direction. In the stages of deceleration and constant velocity development of radial strain variation, the difference in $\Delta\varepsilon_3$ at different positions seems more obvious than that of $\Delta\varepsilon_1$. For instance, the values of strain gauges R4 and R5 on L2 observation plane do not change significantly during the test, and there are no typical stages of deceleration, constant velocity and accelerated development of creep. The strain value at R5 even shows a slight rise, while the strain values at other positions basically conform to the law of strain development in the three stages of creep until the failure, although a certain difference in the change rate has observed. The literature [21] suggests that the fracture dislocation during creep also undergoes deceleration, constant velocity and acceleration three stages. Meanwhile, the strain evolution rule at different locations in the creep process does not completely follow the law of deceleration, constant velocity and acceleration creep stages, but is related to whether the upcoming macro cracks pass through the region.

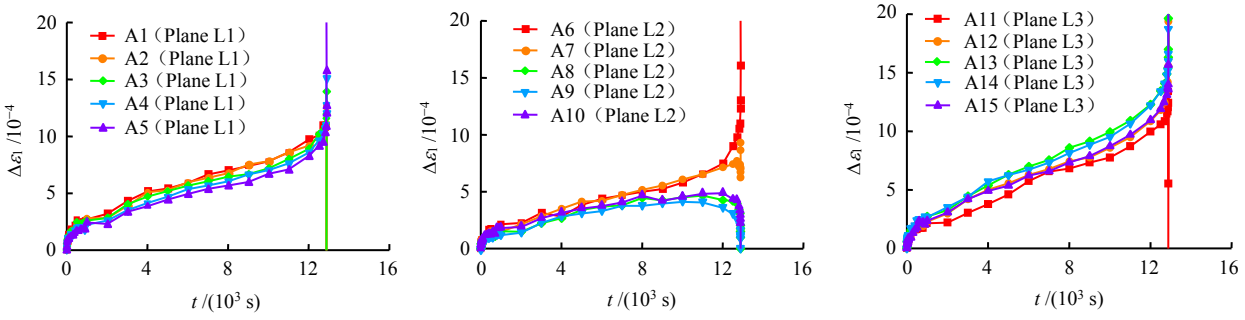

(a) Observation plane L1 (b) Observation plane L2 (c) Observation plane L3

Fig. 9 $\Delta\varepsilon_1$-t curves measured by different axial virtual strain gauges in generalized relaxation tests (α=∞)

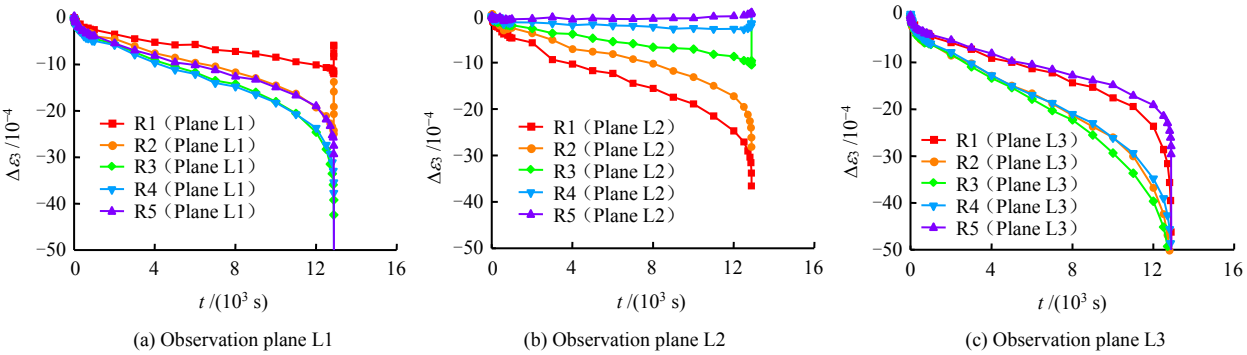

(a) Observation plane L1 (b) Observation plane L2 (c) Observation plane L3

Fig. 10 $\Delta\varepsilon_3$-t curves measured by different radial virtual strain gauges in generalized relaxation tests (α=∞)

In order to reflect the evolution difference between axial and radial strain variations at different positions at different time, and to evaluate the comparability of the 15 axial and radial virtual strain gauges that equidistantly distributed on the sample surface, based on the strain changes measured by each virtual strain gauge, isochronous distribution curves of 15 axial and radial strain changes are plotted according to their spatial positions (Fig. 11). The strain values of adjacent positions are connected by means of spline interpolation. As shown in Fig. 11(a), there is apparent difference in $\Delta\varepsilon_1$ of each axial position at 12 000 s. In the following 884 s, this difference gradually becomes obvious along with evolution. On the isochronous curve of 12 000 s, the strains at A8, A9 and A10 present typical "trough". It can be judged that the strains at A8, A9 and A10 will continue to decrease in the subsequent development, while the strains in other regions will continue to increase. In the third stage of creep, the strains at different positions have developed unevenly. In Fig. 11(b), the "trough" of the isochronous curve evolution also shows rebound of strain value after the macroscopic failure appears. Compared with the axial direction, the development trend of the isochronous curve in the radial direction can identify the strain peak region earlier.

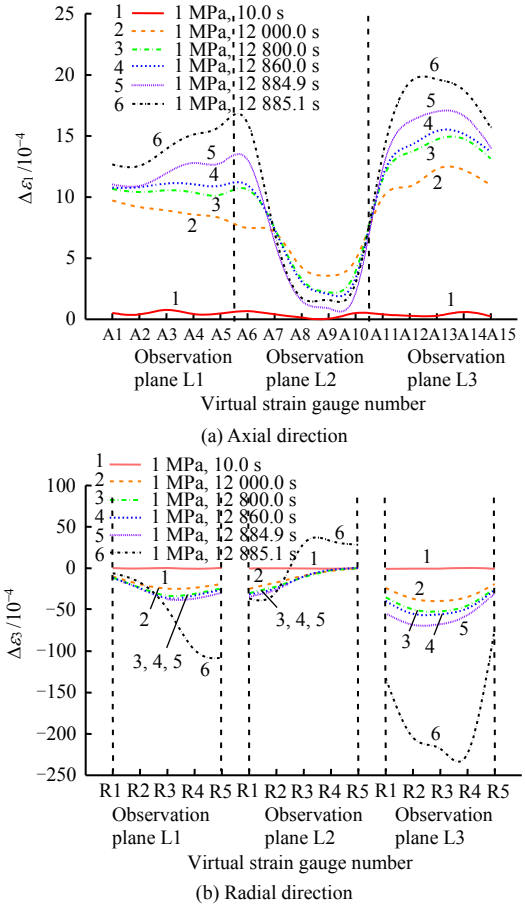

Fig. 11 $\Delta\varepsilon_1$& $\Delta\varepsilon_3$ in isochronous curves measured by virtual strain gauges in generalized relaxation tests (α=∞)

The isochronous curves are obtained by measuring the strain values of the virtual strain gauges at different axial and radial positions. According to the engineering practice, the isochronous curves that measured at different positions of the rock mass at equal distance can be used to judge the area where the rock mass may be fail or strain rebound in advance, so as to improve the reliability of rock mass support.

The axial and radial strain values on the evolution contours of axial and radial strain fields are output, and then the evolution rule of the mean and variance of the overall strain variation in axial and radial strain fields can be obtained through analysis and statistics, as shown in Figs. 12 and 13. As the direction coefficient evolves from 0.3 to 0, −3.0, ∞ and 3.0, the mean value of the variation of the axial strain field gradually increases from negative to positive over time, which is similar to the variation rule of axial strain measured by LVDT in Fig. 5. Meanwhile, the variance of axial strain field $S(\Delta\varepsilon_1)$ at each time is also sorted in the order of α= 3.0, ∞, −3.0, 0, 0.3, respectively. Variance can represent the inhomogeneity of strain development on the surface of sandstone, which essentially reflects the strain localization region that is gradually formed on the surface of sandstone. The mean value $\Delta\bar{\varepsilon}_3$ and variance $S(\Delta\varepsilon_3)$ of the variation in radial strain field are similar to those of $\Delta\bar{\varepsilon}_1$ and $S(\Delta\varepsilon_1)$ of axial direction. The direction coefficient is in the order of 0.3、0、−3.0、∞、3.0, respectively. The $\Delta\bar{\varepsilon}_3$ gradually evolves from positive to negative value over time. In the comparison, the evolution rule of $S(\Delta\varepsilon_3)$ is basically consistent with that of $\Delta\bar{\varepsilon}_3$.

Through the above quantitative analysis, it is found that if the sandstone has a tendency to be fractured during the rheological process, within a certain range where the crack is about to form, the strain development rate will experience the stages of deceleration, constant velocity and acceleration, whereas the strain far away from the cracks may increase marginally at first and then decrease. The evolution rates of strain variations between different regions are similar to the three change stages experienced by the whole region. The changes of mean value and variance are affected by rheological direction and evolve from α=0.3 to 0, −3.0, ∞ and 3.0, successively. In other words, they evolve counterclockwise from the direction of unloading curve of sandstone to the direction of loading. The evolution rate is gradually accelerated, and the sandstone is more likely to be fractured in the process of rheology.

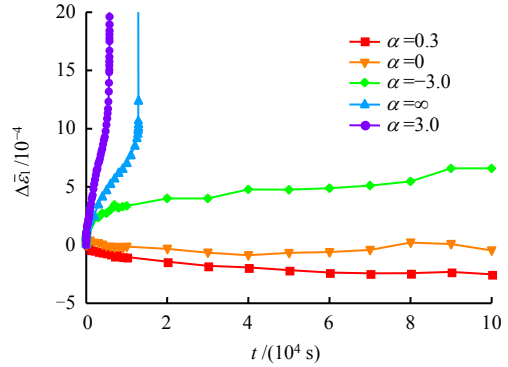

(a) Mean of the axial strain field variation

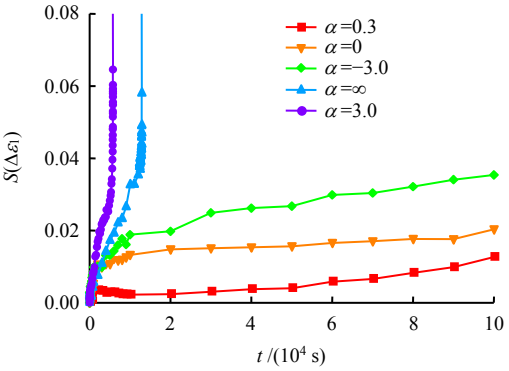

(b) Variance of the axial strain field variation

Fig. 12 Mean and variance of axial strain variation of sandstone in generalized relaxation tests

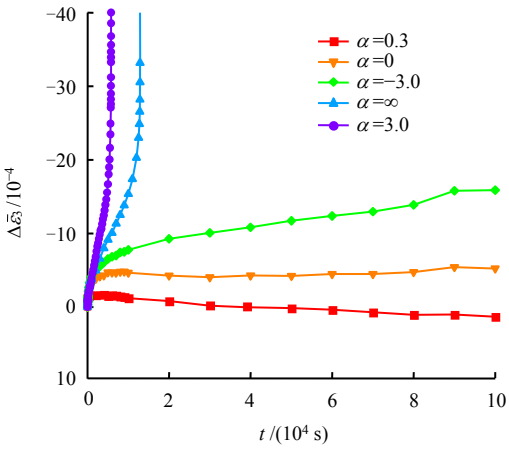

(a) Mean of the radial strain field variation

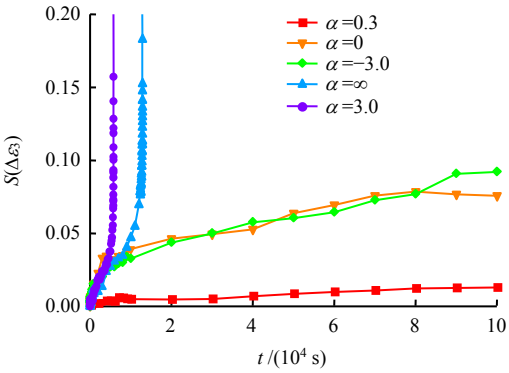

(b) Variance of the radial strain field variation

Fig. 13 Mean and variance of radial strain variation of sandstone in generalized relaxation tests

4 Conclusions

Based on the visual triaxial compression servo control test system and 3D-DIC technology, the generalized stress relaxation tests were carried out to analyze the evolution rule of the strain field on the surface of sandstone. The main conclusions can be drawn as follows:

(1) In the process of generalized stress relaxation of sandstone, the larger strain region of the surface axial strain field at the initial rheological stage presents a layered distribution, while the strain distribution of the radial strain field is more uniform. If the sandstone has a tendency of failure, the strain concentration region of the axial strain field gradually concentrates and connects to the position where the cracks are about to occur, whereas the strain evolution rate of the radial strain field decreases outward from the cracks center.

(2) During the rheological process, the differences between the evolution rates of axial and radial strain values at different sandstone surface positions are positively correlated with the change of the overall strain value. If the rock sample tends to fail, the strain development near the cracks follows the pattern of deceleration, constant velocity and acceleration, while the strain evolution far away from the cracks tends to increase first and then decrease. The isochronous evolution curve of strain values at different positions can be used to determine the potential fracturing area.

(3) Under the same starting axial stress level, as the rheological direction coefficient changes from 0.3 to 0, −3.0, ∞ and 3.0, successively (evolves counterclockwise from the direction of unloading curve of sandstone to the direction of loading). The mean value and variance of axial and radial strain fields increase with time, accompanied with the increasing overall evolution rate. The strain concentration trend is more significant and the change is more dramatic before the failure of the sample.

References

[1] SUN Jun. Rheological mechanics of geo-materials and its engineering application[M]. Beijing: China Architecture and Building Press, 1999.

[2] LIU Xiong. An introduction to rock rheology[M].Beijing: Geological Publishing House,1994.

[3] QIAN Qi-hu, LI Shu-chen. A review of research on zonal disintegration phenomenon in deep rock mass engineering[J]. Chinese Journal of Rock Mechanics and Engineering, 2008, 27(6): 1278−1284.

[4] HUANG Bing-xiang, ZHANG Nong, JING Hong-wen, et al. Large deformation theory of rheology and structural instability of the surrounding rock in deep mining roadway[J].Journal of China Coal Society, 2020, 45(3):

911−926.

[5] OKUBO S, FUKUI K, HASHIBA K. Long-term creep of water-saturated tuff under uniaxial compression[J]. Intenational Journal of Rock Mechanics & Mining Sciences, 2010, 47(5): 839−844.

[6] MISHRA B, VERMA P. Uniaxial and triaxial single and multistage creep tests on coal-measure shale rocks[J]. International Journal of Coal Geology, 2015, 137: 55−65.

[7] ZHANG Yu, XU Wei-ya, SHAO Jian-fu, et al. Experimental investigation on rheological properties and permeability of clastic rock under hydro-mechanical coupling[J]. Chinese Journal of Rock Mechanics and Engineering, 2014, 33(8): 1679−1690.

[8] PARASKEVOPOULOU C, PERRAS M, DIEDERICHS M, et al. The three stages of stress relaxation-observations for the time-dependent behaviour of brittle rocks based on laboratory testing[J]. Engineering Geology, 2017, 216(12): 56−75.

[9] TANG Li-zhong, PAN Chang-liang. Experiment study on properties of stress relaxation of rock under deformation at peak load[J]. Rock and Soil Mechanics, 2003, 24(6): 940−942.

[10] YU Huai-chang, ZHAO Yang, LIU Han-dong, et al. Experimental study of influence of water on stress relaxation of rock under triaxial stress[J]. Chinese Journal of Rock Mechanics and Engineering, 2015, 34(2): 313−322.

[11] LIU Zhi-yong, XIAO Ming-li, XIE Hong-qiang, et al. Stress relaxation properties of schist based on damage evolution[J]. Rock and Soil Mechanics, 2016, 37(Suppl.1): 101−107.

[12] ZHANG Long, LIU Yao-ru, YANG Qiang, et al. A viscoelastic-viscoplastic constitutive equation of rock materials based on irreversible internal variable thermos-dynamics[J]. Engineering Mechanics, 2015, 32(9): 34−41.

[13] XIONG Jun-min, LI Zuo-qin. Creep-stress relaxation coupling experimental study in clay[J]. Rock and Soil Mechanics, 1993, 14(4): 17−24.

[14] FUKUI K, OKUBO S, NISHIMATSU Y. Generalized relaxation behaviour of rock under uniaxial compression[J]. Journal of the Mining and Materials Processing Institute of Japan, 1992, 108(7): 543−548.

[15] HASHIBA K, FUKUI K. Time-dependent behaviors of granite: loading-rate dependence, creep, and relaxation[J]. Rock Mechanics and Rock Engineering, 2016, 49(7): 2569−2580.

[16] XU Jiang, MA Tian-yu, SEISUKE Okubo, et al. Experimental study of generalized stress relaxation characteristics of rock under different confining pressures[J]. Rock and Soil Mechanics, 2017, 38(Suppl.2): 57−64.

[17] XING H Z, ZHANG Q B, RUAN D, et al. Full-field measurement and fracture characterisations of rocks under dynamic loads using high-speed three-dimensional digital image correlation[J]. International Journal of Impact Engineering, 2018, 113: 61−72.

[18] MUNOZ H, TAHERI A, CHANDA E K. Pre-peak and post-peak rock strain characteristics during uniaxial compression by 3D digital image correlation[J]. Rock Mechanics and Rock Engineering, 2016, 49(7): 2541−2554.

[19] TANG Y, OKUBO S, XU J, et al. Progressive failure behaviors and crack evolution of rocks under triaxial compression by 3D digital image correlation[J]. Engineering Geology, 2019, 249:172−185.

[20] WANG Xue-bin, HOU Wen-teng, PAN Yi-shan, et al. Experiments of strain localization processes of coal specimens in uniaxial compression based on the digital image correlation method[J]. Journal of China Coal Society, 2018, 43(4): 984−992.

[21] SONG Yi-min, ZHAO Tong-bin, JIANG Yao-dong. Experimental study on the evolution of creep deformation field of rock based on DSCM[J]. Journal of China University of Mining & Technology, 2013, 42(3): 466−470.

[22] TANG Yang. Time-dependent behaviour of rocks under triaxial compression condition[D]. Chongqing: Chong-qing University, 2018.

[23] SEISUKE Okubo, TANG Yang, XU Jiang, et al. Application of 3D-DIC system in rock mechanic test [J]. Rock and Soil Mechanics, 2019, 40(8): 3263−3273.

[24] SONG Yi-min, DENG Lin-lin, LÜ Xiang-feng, et al. Study of acoustic emission characteristics and deformation evolution during rock frictional sliding[J]. Rock and Soil Mechanics, 2019, 40(8): 2899−2906.